SCIENTIFIC REPORTS

OPEN

Large area growth of $MoTe_2$ films as high performance counter electrodes for dye-sensitized solar cells

Received: 7 July 2017
Accepted: 4 December 2017
Published online: 08 January 2018

Sajjad Hussain[1,2], Supriya A. Patil[3,4], Dhanasekaran Vikraman[5], Naveed Mengal[6], Hailiang Liu[1,2], Wooseok Song[7], Ki-Seok An[7], Sung Hoon Jeong[6], Hak-Sung Kim[3,4] & Jongwan Jung[1,2]

A cost effective and efficient alternative counter electrode (CE) to replace commercially existing platinum (Pt)-based CEs for dye-sensitized solar cells (DSSCs) is necessary to make DSSCs competitive. Herein, we report the large-area growth of molybdenum telluride ($MoTe_2$) thin films by sputtering-chemical vapor deposition (CVD) on conductive glass substrates for Pt-free CEs of DSSCs. Cyclic voltammetry (CV), Tafel curve analysis, and electrochemical impedance spectroscopy (EIS) results showed that the as-synthesized $MoTe_2$ exhibited good electrocatalytic properties and a low charge transfer resistance at the electrolyte-electrode interface. The optimized $MoTe_2$ CE revealed a high power conversion efficiency of 7.25% under a simulated solar illumination of 100 mW cm^{-2} (AM 1.5), which was comparable to the 8.15% observed for a DSSC with a Pt CE. The low cost and good electrocatalytic properties of $MoTe_2$ thin films make them as an alternative CE for DSSCs.

Dye-sensitized solar cells (DSSCs) are gaining considerable interest for next-generation photovoltaic devices due to their acceptable energy conversion efficiency, low cost, environmental friendliness, and easy fabrication processes[1,2]. Typically, DSSCs have a sandwich structure with a photoanode (a semiconductor film on an FTO substrate sensitized by dye molecules), an electrolyte containing the iodide/triiodide (I^-/I_3^-) redox couple, and a counter electrode (CE) catalyzing the reduction of I_3^- to I^-. Platinum (Pt) is an excellent catalyst for the reduction of I_3^- to I^- due to its superior conductivity, electrocatalytic activity, and stability[3,4]. However, Pt is a noble metal and it is scarce and expensive. Therefore, new materials have been explored to develop cost-effective Pt-free CEs for DSSCs. To date, numerous attempts have been made to find alternative CEs, including transition metal dichalcogenides (TMDC), carbon materials, conducting polymers[5,6], nitrides[7,8], and carbides[9,10]. In particulary, interests in 2D materilas such as TMDC materials including selenides and sulphides are high because of their good electrocatalytic activity and stability[11–14]. Previously, our group demonstrated that molybdenum disulfide (MoS_2) and tungsten disulfide (WS_2) are good CE materials for DSSCs. They exhibited photovoltaic conversion efficiencies (PCEs) of 6.0% and 6.3%, respectively[15,16]. However, the efficiency is still not satisfactory, and efforts to improve the efficiency and discover a new TMDC materials are ongoing. Recently, tellurides such as WTe_2 and $MoTe_2$ in the family of TMDC materials are gaining interests in electronic and optoelectronic devices[17–19]. Like other TMDC materials, the band gap of $MoTe_2$ also depends on the number of layers. $MoTe_2$ has an lowest indirect band gap of ~1.0 eV, and single-layer $MoTe_2$ is a direct gap material with an optical band gap of 1.1 eV[20], close to that of Si (1.1 eV)[21]. $MoTe_2$ has a low band gap in the family of TMDC materials. $MoTe_2$ crystal is highly stable

[1]Graphene Research Institute, Sejong University, Seoul, 143-747, Republic of Korea. [2]Institute of Nano and Advanced Materials Engineering, Sejong University, Seoul, 143-747, Republic of Korea. [3]Department of Mechanical Engineering, Hanyang University, Haengdang-dong, Seongdong-gu, 133-791, Seoul, Republic of Korea. [4]Institute of Nano Science and Technology, Hanyang University, Seoul, 133-79, Republic of Korea. [5]Division of Electronics and Electrical Engineering, Dongguk University-Seoul, Seoul, 04620, Republic of Korea. [6]Department of Organic and Nano Engineering, Hanyang University, Seoul, 133-791, Republic of Korea. [7]Thin Film Materials Research Group, Korea Research Institute of Chemical Technology, Daejon, 305-600, Korea. Sajjad Hussain and Supriya A. Patil contributed equally to this work. Correspondence and requests for materials should be addressed to H.-S.K. (email: kima@hanyang.ac.kr) or J.J. (email: jwjung@sejong.ac.kr)

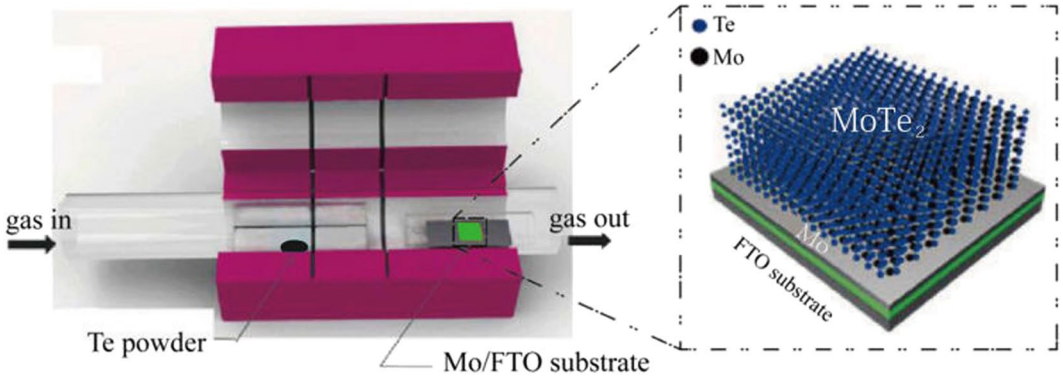

Figure 1. Schematic illustration of tellurization for the preparation of $MoTe_2$ from Mo/FTO substrate using a two-zone chemical vapour deposition chamber.

in semiconducting (2 H) and metallic (1 T′) phase in nature[22,23]. The hydrogen evolution reaction catalytic activity of $MoTe_2$ was reported[24]. In this work, we report the catalytic activities of $MoTe_2$ as counter electrode in DSSCs.

Herein, we have grown $MoTe_2$ thin films *via* sputtering combined with a post-deposition annealing process on conductive glass substrates with different thickness. This work is a continuation of our research focusing on TMDC material search and growth for DSSC applications. $MoTe_2$ films used as CEs in DSSC showed good electrical conductivity and electrocatalytic activity, and a DSSC employing a $MoTe_2$ CE synthesized under optimized conditions had a 7.25% PCE, which is comparable to the value of 8.15% obtained for the Pt CE under the same conditions. To the best of our knowledge, this is the highest PCE for (I^-/I_3^-) redox couple-based DSSCs employing $MoTe_2$ CE under a simulated solar illumination of 100 mW·cm^{-2} (AM 1.5).

Results and Discussion

In this study, we fabricated large-area and high-quality $MoTe_2$ directly onto FTO substrate by sputtering-CVD growth, as depicted in Fig. 1. Our synthesis method consists of two steps. Initially, Mo films were deposited onto FTO substrates using magnetron sputtering, and the film was annealed at 500 °C in a tellurium environment in a CVD chamber. Three samples were sputtered at three different times (20, 30, and 40 min) and subsequently tellurized, and referred to S1 (~185 nm), S2 (~335 nm), and S3 (~668 nm), respectively.

Field emission scanning electron microscopy (FE-SEM) analysis was performed to reveal the surface morphology of the $MoTe_2$/FTO structure. Figure 2(a–c) provide FE-SEM images of samples S1, S2 and S3, respectively. Samples exposed to the longest tellurization (40 min) exhibits the biggest grains in Fig. 2(c). Cross-sectional SEM images show that the thicknesses of the S1, S2 and S3 are ~185, ~355 and ~688 nm, respectively (Fig. 2d–f). The low magnification FE-SEM image with EDS spectrum for the sample S2 is provided in supporting information (Figure S1a,b). The cross-sectional view with their EDS profile is provided to confirm the presence of Mo and Te in the $MoTe_2$ film (Figure S1c,d).

The structures of the $MoTe_2$ films were characterized by Raman spectroscopy using a 514 nm excitation laser. Figure 3(a) shows prominent peaks at ~161, and ~267 cm^{-1}, which correspond to the A_g mode. A shoulder peak was observed at ~189 cm^{-1}, and this was ascribed to the B_g mode, for $MoTe_2$ in the 1 T′ phase. The spectrum agrees well with the previously reported results[22,25]. XRD measurements were performed to further evaluate the identity and structure of the film, as shown in Fig. 3b. The XRD patterns show that the synthesized $MoTe_2$ films were polycrystalline in nature with a monoclinic structure. The diffraction peaks were at 38.0°, 42.7°, 51.7°, 54.7°, 61.7°, 64.7°, 65.9°, 71.2°, and 78.8°, which correspond to (210), (106), (311), (022), (221), (411), (125), ($\bar{2}$19), and ($\bar{5}$04) lattice planes of $MoTe_2$, respectively (JCPDS No. 71–2157). No impurities or other reflections from deleterious crystalline phases were observed, which suggests that well oriented $MoTe_2$ films were deposited.

X-ray photoemission spectroscopy (XPS) was used to verify the surface chemical compositions and valence states of 1 T′-$MoTe_2$. The survey spectrum indicates the coexistence of Mo and Te elements in the $MoTe_2$ films (Figure S2). High-resolution spectra of each element are also given in Fig. 4a,b. As shown in Fig. 4a, the Mo 3d spectrum exhibits two main peaks at 229.2 and 232.2 eV, corresponding to the doublet of Mo $3d_{5/2}$ and Mo $3d_{3/2}$. For Te 2d specturm, peaks were observed at 573.1 and 583.6 eV, as shown in Fig. 4b. These can be assigned to the spin–orbit couple of Te $2d_{5/2}$ and Te $2d_{3/2}$, respectively[18]. The stoichiometry of Mo and Te elements in our synthesized $MoTe_2$ film is confirmed by EDS spectrum (Fig. S1b). Hall measurements were performed on $MoTe_2$/glass at room temperature (RT) with an active area of (1 × 1) cm^2 (Figure S3). $MoTe_2$ CE revealed p-type behavior similar to that reported in the literature[26]. The conductivity = 3.3×10^{-1} Ω^{-1}cm^{-1}, and charge mobility = 95 cm^2 V^{-1} s^{-1} were extracted from the device.

To investigate the application of the $MoTe_2$ as a CE in DSSCs, cyclic voltammetry (CV) studies were performed to estimate the reaction kinetics and electrocatalytic performance. CV was conducted using a three-electrode system in an acetonitrile solution consisting of 10 mM LiI, 1 mM I_2, and 0.1 mM $LiClO_4$ at a scan rate of 20 mVs^{-1}. Figure 5a shows the CVs of the system for Pt and $MoTe_2$ (S1, S2, S3) in the potential interval between −0.2 to 1 V vs. Ag/AgCl. The Ox_1 and Red_1 peaks at low potential were attributed to the redox reaction of $I_3^- + 2e^- \leftrightarrow 3I^-$. The Red_1 peak corresponding to $I_3^- + 2e^- \leftrightarrow 3I^-$ was used to evaluate the integral electrocatalytic ability of CEs to reduce triiodide ions to iodide ions. This reduction occurs in DSSCs, and the current density of this

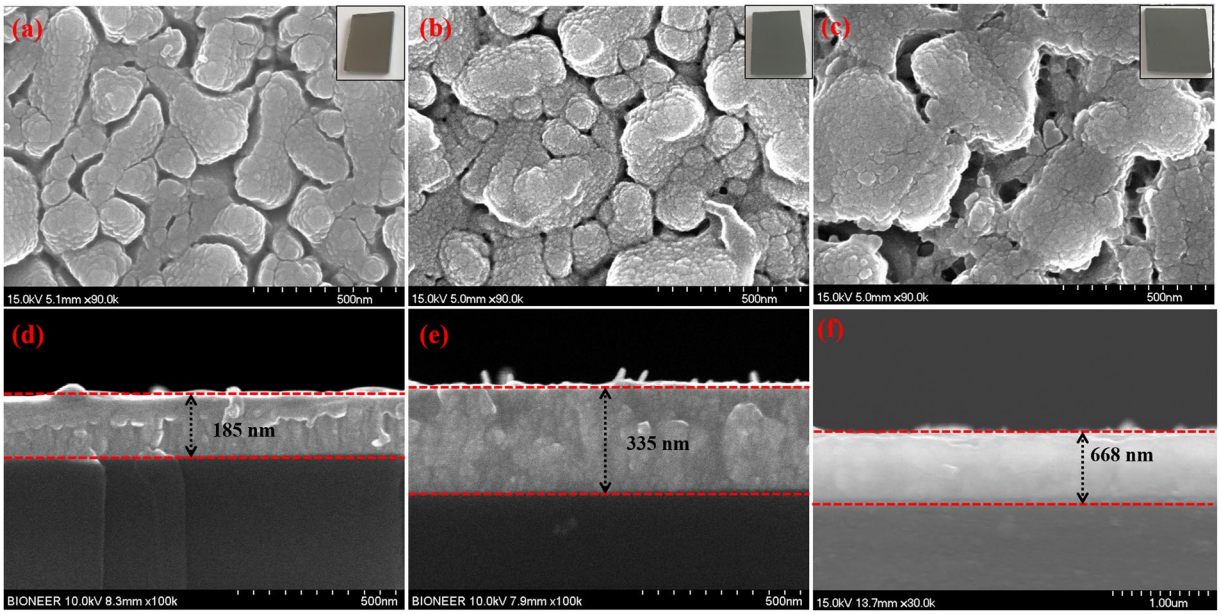

Figure 2. (**a–c**) Top down FE-SEM images of S1, S2 and S3 (Inset shows the corresponding image of $MoTe_2$ sample) and (**d–f**) cross-sectional images of S1, S2 and S3. The observed thickness were ~185 nm, ~335 nm and ~ 668 nm for S1, S2 and S3, respectively.

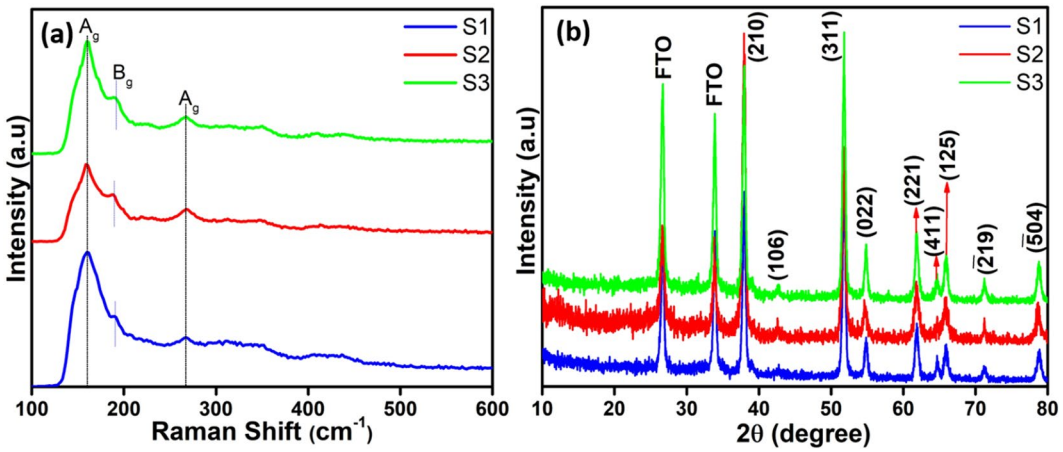

Figure 3. (**a,b**) Raman spectra and XRD patterns of $MoTe_2$ samples.

reaction is mainly determined by the number of reduction-active sites on the surface area of the electrocatalyst and the intrinsic electrocatalytic ability of each site. Ox_1 and Red_1 represent the same electrochemical reaction $I_3^- + 2e^- \leftrightarrow 3I^-$, in which Ox_1 indicates the left direction and Red_1 indicates the right direction.

CV curves show that, like Pt, S1 and S2 also are catalytically active for the reaction that regenerates the redox couple. The higher cathodic peak current density can be used to evaluate the catalytic activity of the CE, and comparable peak current densities imply good electrocatalytic activity. The ~335 nm-thick (S2) CE showed higher current density than the ~185 nm CE (S1), suggesting faster reduction of triiodide ions in the S2 CE compared to the S1 CE (Fig. 4a). The higher cathode current density could be attributed to its relatively higher surface roughness compared to the much smoother S1. Furthermore, S1 and S2 samples displayed similar anodic and cathodic peaks to Pt CE, suggesting that they are active in catalyzing the reduction of I_3^- to I^-. The peak current and peak to peak separation is important parameters for determining the catalytic activity of CE. The rate constant of a redox reaction is inversely proportional to its peak separation (Epp)[27–29]. Epp is calculated using the formula

$$\text{Epp} = \text{Ep(anodic)} - \text{Ep(cathodic)} \quad (1)$$

In DSSCs, the CE has more influence on the negative peak. So, we used this peak for Epp calculations. The Epp for the Pt CE was 295 mV, while those for S1, S2 and S3 were ~354, ~459 and ~308 mV, respectively.

To investigate the electrochemical stability of $MoTe_2$ S2 sample and Pt CE, CVs were recorded for 50 consecutive cycles with a potential range from −0.2 to 1 V vs. Ag/AgCl, as presented in Figure S4a. After 50 consecutive

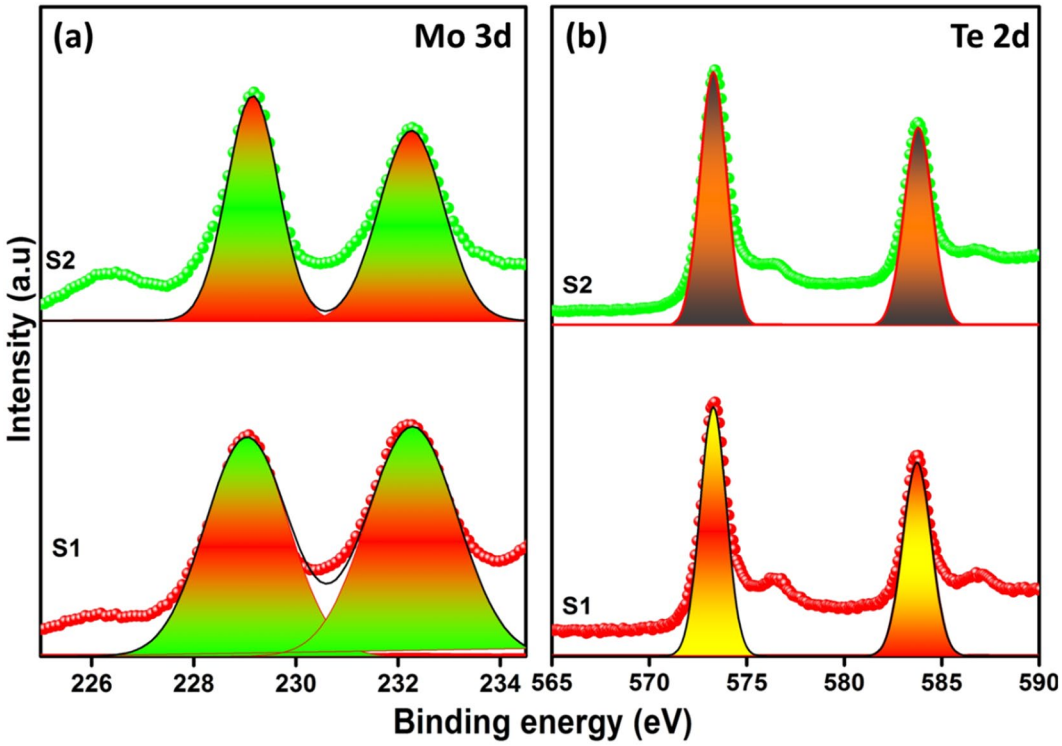

Figure 4. **(a,b)** XPS spectra of $MoTe_2$ samples (**a**) Mo atoms and (**b**) Te atoms of S1 and S2, respectively.

scans, the CV shape of sample S2 almost overlapped, and the redox peak current (cathodic and anodic peak current density) for sample S2 was almost constant, which suggests that the $MoTe_2$ CE possesses reversible redox activity, good electrochemical and chemical stability, and strong adhesion on the FTO glass substrate. The CVs of sample S1, S2 and S3 were measured using different scan rates from 10 to 100 mVs^{-1} for the (I^-/I_3^-) redox reaction, as shown in Figure S4b–d, respectively. There are a linear increment in the current peak value with increasing scan rate, indicating that the inner sites of $MoTe_2$ also become reactive and possess catalyst activity at higher scan rate[29,30].

To further evaluate the charge transfer kinetics and internal resistance of DSSCs, EIS measurements were performed using symmetric cells fabricated with two identical electrodes (CE/electrolyte/CE). The equivalent circuit model used for fitting the resultant impedance data is illustrated in Fig. 5b. In each curve, there are two well-defined semicircles. The first semicircle at high frequency is related to impedance of charge transfer process occuring at CE/electrolyte and lower frequency range can be assigned to the Nernst diffusion impedance (Z_w) within electrolyte. The extracted charge–transfer resistance (R_{ct}) values of the Pt, S1, S2 and S3 CEs are 0.93, 27.01, 25.97, and 37.44 Ω cm^2, respectively. The sample S3 has the largest R_{ct} and S2 has the lowest one among the $MoTe_2$ samples. R_s values of S1, S2, S3 and Pt are 16.47, 13.79, 13.83, and 7.05 Ω cm^2, respectively. The sample S2 has the lowest R_s. The R_s value of S3 is largest probably due to the largest film thickness.

Tafel polarization analyses were also performed using symmetric cells at a scan rate of 50 mVs^{-1} for Pt, S1, S2 and S3 samples (Fig. 5d). The Tafel curve is usually divided into three regions. The lower potential zone is called the polarization zone, and the middle region (with a sharp slope) is the Tafel zone, which determines the catalytic activity of the electrode. The last zone is the diffusion zone, which determines the diffusion of ions in the electrode. The tangent slope in the anodic or cathodic branch provides information about the exchange current density (J_0) on the electrode[31]. The comparison indicates that S2 (S2 > S1 > S3) is more effective than S1 and S3 at catalyzing the reduction of I_3^-. The exchange current density, J_0 is inversely proportional to R_{ct} from the equation

$$J_0 = (RT/nFR_{ct}) \quad (2)$$

where R is a gas constant, T is an absolute temperature, n is the number of electrons involved in the reaction, and F is Faraday's constant[27,32]. A higher J_0 for Pt and S2 CE implies a lower value of R_{ct} in the impedance measurement.

The schematic of DSSCs with MoTe CE is illustrated in Fig. 6a. The photocurrent density *versus* photovoltage (J-V) curves of the DSSCs are shown in Fig. 6b. The photovoltaic paramters including the short circuit current density (J_{sc}), open circuit voltage (V_{oc}), fill factor (FF) and PCE (η) of DSSCs with Pt and $MoTe_2$ (S1, S2 and S3) CEs under a simulated solar illumination of 100 $mWcm^{-2}$ (AM 1.5) are summarized in the Table 1. The sample S2 CE exhibits the best performnce. The DSSC with S1 CE has lower FF than that with S2 CE, which is related to red-ox behaviour as discussed in earlier. The J_{sc} and FF values are increased for the S2 CE, which leads to enhancing PCE from 6.38% to 7.25%. And, the low efficency of S3 CE is mainly due to low V_{oc} and FF. This could be attributed to higher R_{ct} value as confirmed by EIS analysis.

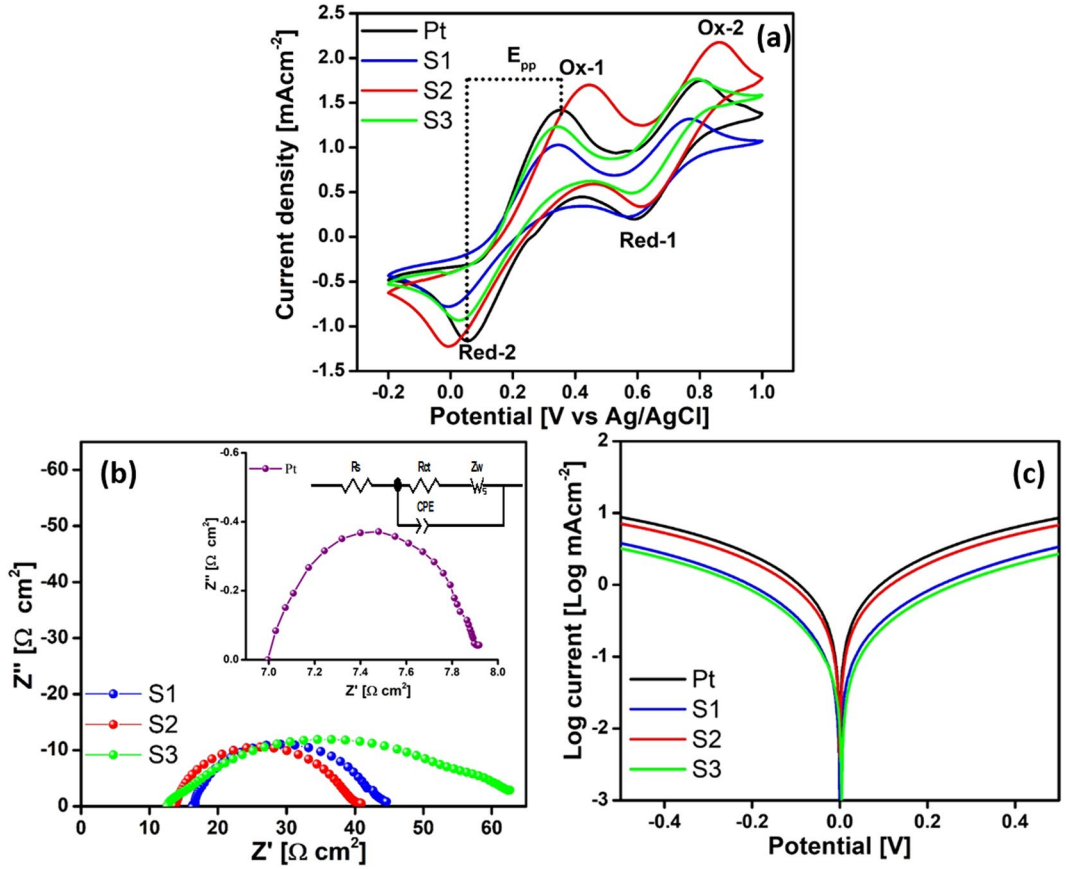

Figure 5. (**a**) CV curves of CEs (scan rate of 20 mVs^{-1}). (**b**) Nyquist plots of the symmetrical cells; Inset – equivalent circuit and Nyquist plot of symmetrical cell with Pt (R_{ct}: charge transfer resistance, Z_w: diffusion impedance, R_s: ohmic internal resistance, CPE: constant phase element). (**c**) Tafel polarization curves of symmetrical cells.

The J_{sc} values are decreased in the order of S3 > S2 > S1 > Pt, and PCE values are decreased in the order of Pt > S2 > S3 > S1. It is believed that thick film (S3) could affect electrolyte penetration and result in weaker adhesion to the FTO substrate[33].

The observed PCE (7.25%) value of the S2 CE was much higher than those of earlier reports based on TMDCs, which include WS_2 films prepared by a doctor-blading technique (4.56%)[34], multi-walled carbon nanotubes-MWCNTs@MoS_2 (6.45%)[35], multi-wall carbon nanotubes decorated with tungsten sulfide-MWCNTs@WS_2 (6.41%)[36], composite films of molybdenum disulfide (MoS_2)/graphene flakes (5.98%)[29], and molybdenum disulfide and graphene-MoS_2/RGO (6.04%)[37]. The variations of V_{oc} and J_{sc} values for $MoTe_2$ and Pt CEs can be attributed to the nanoporous nature of the $MoTe_2$ CE in contrast to the planar Pt CE, and the high conductivity of Pt. Figures S5 shows incident photon-to current-conversion efficiency (IPCE) curves of DSSCs with the $MoTe_2$ CE and Pt CE. These results indicate that catalytic activities depend on the $MoTe_2$ thickness since active sites and morphology vary with the growth time, supporting that catalytic activities of thin $MoTe_2$ could be modulated by their film thickness and morphology.

Conclusions

In summary, we presented the sputtering-CVD post annealing route for synthesizing $MoTe_2$ as counter electrodes for DSSCs. Detailed electrochemical investigations were carried out using cyclic voltammetry, electrochemical impedance spectroscopy, and Tafel curve analysis to determine the suitability for CE for DSSCs. CV performance revealed that $MoTe_2$ CEs possess good electrocatalytic activity and fast reaction kinetics for the reduction of triiodide to iodide. It was found that catalytic activities of thin $MoTe_2$ could be modulated by their film thickness and morphology.

The optimum $MoTe_2$ CE in a fabricated DSSC exhibited a 7.25% PCE, which is comparable to the 8.15% Pt CE under the same illumination conditions. The presented work suggests that $MoTe_2$ would be a promising counter electrode material as a low-cost and highly efficient alternative to Pt in DSSCs.

Experimental Section and Device preparation. FTO/glass substrates were cleaned with a standard piranha solution and deionized water and were then baked at 120 °C for 5 min. After loading the FTO substrates in a sputter chamber, the chamber was evacuated by a rotary pump and a turbomolecular pump combination to a pressure of ~1×10^{-7} torr. Next, Mo thin films were deposited onto FTO/glass substrates using a Mo target

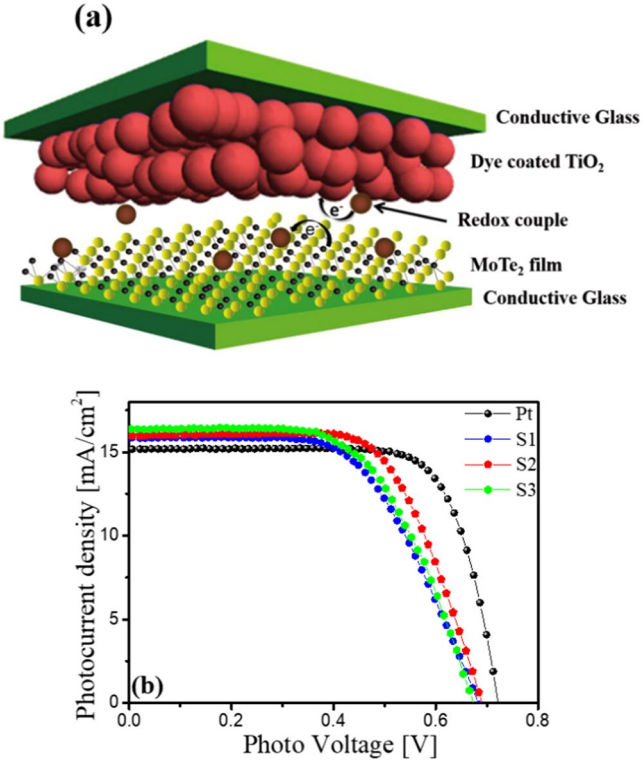

Figure 6. (**a**) Schematic diagram of the electrocatalytic mechanism in DSSC using $MoTe_2$ CE. (**b**) Photocurrent–voltage curves of DSSCs with different CEs, measured at AM1.5 G illumination (100 mW cm^{-2}).

Name of CEs	V_{oc} (V)	J_{sc} (mA cm^{-2})	*FF* %	PCE (η)%	R_S (Ω cm^2)	R_{ct} (Ω cm^2)	Z_W (Ω cm^2)
Pt	0.72	15.18	74.37	8.15	7.05	0.93	0.99
S1	0.68	15.84	58.98	6.38	16.47	27.01	27.56
S2	0.69	16.00	65.64	7.25	13.79	25.97	27.51
S3	0.67	16.37	59.50	6.55	13.83	37.44	52.08

Table 1. Photovoltaic and EIS parameters of Pt, S1, S2 and S3 based DSSC CEs.

(99.99%) by magnetron sputtering. During the film deposition, the Ar gas flow ratio was maintained at 10 sccm, and the power was fixed at 100 W. Mo films were deposited at different sputtering times (such as 20, 30, and 40 min) at room temperature, and these are denoted as S1 (185 nm), S2 (335 nm), and S3 (668 nm) samples, respectively. After removing the samples from the sputter chamber, the as-sputtered films were placed downstream of the chemical vapor deposition (CVD) chamber and heated. The as-sputtered Mo films were annealed in tellurium vapor at 500 °C for 30 min to form $MoTe_2$ films and to improve the crystalline quality of the films. A pure tellurium powder (99.99%) was placed upstream of the CVD chamber, and a heating filament for the tellurium boat was fixed at 350 °C. The tellurium powder was evaporated at 350 °C using a mixture of argon and hydrogen (60 sccm - Ar and 30 sccm - H_2) carrier gases, and the pressure of the CVD chamber was kept at 2×10^{-2} Torr.

Fabrication of DSSCs. DSSCs were fabricated to evaluate the CE performance of the $MoTe_2$ films using our method[38–41]. Briefly, thin blocking layer TiO_2 was deposited onto a cleaned FTO glass substrate (15×15 mm^2) by dipping it in 40 mM $TiCl_4$ solution for 30 min at 70 °C and annealing it at 450 °C for 30 min. A homemade titanium dioxide (TiO_2) powder paste of P25 was coated on the cleaned FTO glass as the main layer (~12 µm thickness) using a simple doctor blade coating technique. The TiO_2-coated FTO was then sintered in five steps of 70, 325, 375, 450, and 500 °C for 30, 5, 5, 15, and 15 min, respectively, in a high temperature furnace (Lab House Co.). Additionally, a scattering layer (~6 µm) was coated over the main layer and sintered using the same sintering steps. The TiO_2 film was then sensitized with 0.5 mM N 719 prepared in an absolute ethanol: acetonitrile (1:1) solution for 24 h. The polymer electrolyte, which was composed of 0.5 M LiI, 0.6 M 1-propyl-2,$_3^-$dimethylimidazolium iodide, 0.05 M I_2, 0.5 M 4-tert-buylpyridine, and 3% w/w polyethylene oxide (Mw 250,000) with acetonitrile as the solvent was then injected between the two electrodes. The Pt-coated CE was prepared by spreading a drop of 2 mM chloroplatinic acid hexahydrate (H_2PtCl_6) in isopropanol onto the FTO substrates using a simple brush method and heating it to 400 °C for 15 min in ambient air[42,43]. The dye-sensitized TiO_2 photoanode with an active area of 0.25 cm^2 and the as-fabricated CE were assembled using a 50-µm-thick spacer made of polyimide adhesive tape.

References

1. O'regan, B. & Grfitzeli, M. A low-cost, high-efficiency solar cell based on dye-sensitized. *Nature* **353**, 737–740 (1991).
2. Grätzel, M. Photoelectrochemical cells. *Nature* **414**, 338–344 (2001).
3. Xin, X., He, M., Han, W., Jung, J. & Lin, Z. Low-Cost Copper Zinc Tin Sulfide Counter Electrodes for High-Efficiency Dye-Sensitized Solar Cells. *Angewandte Chemie International Edition* **50**, 11739–11742 (2011).
4. Kay, A. & Grätzel, M. Low cost photovoltaic modules based on dye sensitized nanocrystalline titanium dioxide and carbon powder. *Solar Energy Materials and Solar Cells* **44**, 99–117 (1996).
5. Xia, J., Masaki, N., Jiang, K. & Yanagida, S. The influence of doping ions on poly (3, 4-ethylenedioxythiophene) as a counter electrode of a dye-sensitized solar cell. *Journal of Materials Chemistry* **17**, 2845–2850 (2007).
6. Lee, K. S., Lee, W. J., Park, N.-G., Kim, S. O. & Park, J. H. Transferred vertically aligned N-doped carbon nanotube arrays: use in dye-sensitized solar cells as counter electrodes. *Chemical communications* **47**, 4264–4266 (2011).
7. Jiang, Q., Li, G., Liu, S. & Gao, X. Surface-nitrided nickel with bifunctional structure as low-cost counter electrode for dye-sensitized solar cells. *The Journal of Physical Chemistry C* **114**, 13397–13401 (2010).
8. Li, G., Song, J., Pan, G. & Gao, X. Highly Pt-like electrocatalytic activity of transition metal nitrides for dye-sensitized solar cells. *Energy & Environmental Science* **4**, 1680–1683 (2011).
9. Wu, M., Lin, X., Hagfeldt, A. & Ma, T. Low-Cost Molybdenum Carbide and Tungsten Carbide Counter Electrodes for Dye-Sensitized Solar Cells. *Angewandte Chemie International Edition* **50**, 3520–3524 (2011).
10. Wu, M. *et al*. Economical Pt-free catalysts for counter electrodes of dye-sensitized solar cells. *Journal of the American Chemical Society* **134**, 3419–3428 (2012).
11. Gong, F., Wang, H., Xu, X., Zhou, G. & Wang, Z.-S. *In situ* growth of Co0. 85Se and Ni0. 85Se on conductive substrates as high-performance counter electrodes for dye-sensitized solar cells. *Journal of the American Chemical Society* **134**, 10953–10958 (2012).
12. Lee, L. T. L. *et al*. Few-layer $MoSe_2$ possessing high catalytic activity towards iodide/tri-iodide redox shuttles. *Scientific reports* **4**, 4063 (2014).
13. Liu, Z., Lau, S. P. & Yan, F. Functionalized graphene and other two-dimensional materials for photovoltaic devices: device design and processing. *Chemical Society Reviews* **44**, 5638–5679 (2015).
14. Yun, S., Hagfeldt, A. & Ma, T. Pt-Free Counter Electrode for Dye-Sensitized Solar Cells with High Efficiency. *Advanced Materials* **26**, 6210–6237 (2014).
15. Hussain, S. *et al*. High-Performance Platinum-Free Dye-Sensitized Solar Cells with Molybdenum Disulfide Films as Counter Electrodes. *ChemPhysChem* **16**, 3959–3965 (2015).
16. Hussain, S. *et al*. Sputtering and sulfurization-combined synthesis of a transparent WS_2 counter electrode and its application to dye-sensitized solar cells. *RSC Advances* **5**, 103567–103572 (2015).
17. Zhang, E. *et al*. Tunable positive to negative magnetoresistance in atomically thin WTe2. *Nano letters* **17**, 878–885 (2017).
18. Zhou, L. *et al*. Large-area synthesis of high-quality uniform few-layer $MoTe_2$. *Journal of the American Chemical Society* **137**, 11892–11895 (2015).
19. Pradhan, N. R. *et al*. Field-effect transistors based on few-layered α-$MoTe_2$. *ACS nano* **8**, 5911–5920 (2014).
20. Ruppert, C., Aslan, O. B. & Heinz, T. F. Optical properties and band gap of single-and few-layer $MoTe_2$ crystals. *Nano letters* **14**, 6231–6236 (2014).
21. Abruna, H., Hope, G. & Bard, A. Semiconductor Electrodes XLV. Photoelectrochemistry of n-and p-Type in Aqueous Solutions. *Journal of The Electrochemical Society* **129**, 2224–2228 (1982).
22. Zhou, J. *et al*. Large-Area and High-Quality 2D Transition Metal Telluride. *Advanced Materials* **29** (2017).
23. Chang, T.-R. *et al*. Prediction of an arc-tunable Weyl Fermion metallic state in MoxW1- xTe2. *Nature communications* **7**, 10639 (2016).
24. Seok, J. *et al*. Active hydrogen evolution through lattice distortion in metallic $MoTe_2$. *2D Materials* **4**, 025061 (2017).
25. Liu, M. *et al*. Synthesis of few-layer 1T′-$MoTe_2$ ultrathin nanosheets for high-performance pseudocapacitors. *Journal of Materials Chemistry A* (2017).
26. Zhou, L. *et al*. Large-area synthesis of high-quality uniform few-layer $MoTe_2$. *J. Am. Chem. Soc* **137**, 11892–11895 (2015).
27. Bhosale, R. K., Agarkar, S. A., Agrawal, I., Naphade, R. A. & Ogale, S. Nanophase CuInS 2 nanosheets/CuS composite grown by the SILAR method leads to high performance as a counter electrode in dye sensitized solar cells. *RSC Advances* **4**, 21989–21996 (2014).
28. Patil, S. A. *et al*. Formation of semimetallic cobalt telluride nanotube film via anion exchange tellurization strategy in aqueous solution for electrocatalytic applications. *ACS applied materials & interfaces* **7**, 25914–25922 (2015).
29. Yue, G., Lin, J.-Y., Tai, S.-Y., Xiao, Y. & Wu, J. A catalytic composite film of MoS_2/graphene flake as a counter electrode for Pt-free dye-sensitized solar cells. *Electrochimica Acta* **85**, 162–168 (2012).
30. Kung, C.-W. *et al*. CoS acicular nanorod arrays for the counter electrode of an efficient dye-sensitized solar cell. *ACS nano* **6**, 7016–7025 (2012).
31. Hauch, A. & Georg, A. Diffusion in the electrolyte and charge-transfer reaction at the platinum electrode in dye-sensitized solar cells. *Electrochimica Acta* **46**, 3457–3466 (2001).
32. Wang, M. *et al*. CoS supersedes Pt as efficient electrocatalyst for triiodide reduction in dye-sensitized solar cells. *Journal of the American Chemical Society* **131**, 15976–15977 (2009).
33. Al-Mamun, M. *et al*. Directly hydrothermal growth of ultrathin MoS_2 nanostructured films as high performance counter electrodes for dye-sensitised solar cells. *RSC Advances* **4**, 21277–21283 (2014).
34. Li, S., Chen, Z. & Zhang, W. Dye-sensitized solar cells based on WS_2 counter electrodes. *Materials Letters* **72**, 22–24 (2012).
35. Tai, S.-Y. *et al*. Few-layer MoS_2 nanosheets coated onto multi-walled carbon nanotubes as a low-cost and highly electrocatalytic counter electrode for dye-sensitized solar cells. *Journal of Materials Chemistry* **22**, 24753–24759 (2012).
36. Yue, G. *et al*. A counter electrode of multi-wall carbon nanotubes decorated with tungsten sulfide used in dye-sensitized solar cells. *Carbon* **55**, 1–9 (2013).
37. Liu, C.-J. *et al*. Facile synthesis of MoS_2/graphene nanocomposite with high catalytic activity toward triiodide reduction in dye-sensitized solar cells. *Journal of Materials Chemistry* **22**, 21057–21064 (2012).
38. Patil, S. A. *et al*. Current density enhancement in ZnO/CdSe photoelectrochemical cells in the presence of a charge separating SnO_2 nanoparticles interfacing-layer. *Dalton Transactions* **42**, 13065–13070 (2013).
39. Arbab, A. A., Sun, K. C., Sahito, I. A., Qadir, M. B. & Jeong, S. H. Multiwalled carbon nanotube coated polyester fabric as textile based flexible counter electrode for dye sensitized solar cell. *Physical Chemistry Chemical Physics* **17**, 12957–12969 (2015).
40. Hussain, S. *et al*. High Performance $MoSe_2$/Mo Counter Electrodes Based-Dye-Sensitized Solar Cells. *Journal of The Electrochemical Society* **164**, E11–E16 (2017).
41. Shinde, D. V. *et al*. Revisiting Metal Sulfide Semiconductors: A Solution-Based General Protocol for Thin Film Formation, Hall Effect Measurement, and Application Prospects. *Advanced Functional Materials* **25**, 5739–5747 (2015).
42. Patil, S. A. *et al*. An ion exchange mediated shape-preserving strategy for constructing 1-D arrays of porous CoS 1.0365 nanorods for electrocatalytic reduction of triiodide. *Journal of Materials Chemistry A* **3**, 7900–7909 (2015).
43. Lim, I. *et al*. Electrocatalytic activity of chemically deposited Cu_xS thin film for counter electrode in quantum dots-sensitized solar cells. *Materials Chemistry and Physics* **148**, 562–568 (2014).

Acknowledgements
This research was supported by the Basic Science Research Program through the National Research Foundation of Korea (NRF), funded by the Ministry of Education (2010–0020207, 2012R1A1A2007211, 2012R1A6A1029029,2016R1D1A1B01015047), and by nano material technology development program through the NRF funded by the Ministry of Science, ICT and Future Planning (2015M3A7B7045194, 2016M3A7B4909942).

Author Contributions
S.H. and D.V. initiated the study, performed the extensive experiments related to the growth of the samples and wrote the paper with assistance from the co-authors. S.A.P. and N.M. carried out electrochemical and solar cell performances. H.L. helped us experimental work and data analyses. W.S. and K.A. performed XPS analyses. H.-S.K., S.H.J. and J. J. participation included planning, design experimental work and discussion. All authors read and approved the final manuscript.

Additional Information
Supplementary information accompanies this paper at https://doi.org/10.1038/s41598-017-18067-6.

Competing Interests: The authors declare that they have no competing interests.

Publisher's note: Springer Nature remains neutral with regard to jurisdictional claims in published maps and institutional affiliations.

Open Access This article is licensed under a Creative Commons Attribution 4.0 International License, which permits use, sharing, adaptation, distribution and reproduction in any medium or format, as long as you give appropriate credit to the original author(s) and the source, provide a link to the Creative Commons license, and indicate if changes were made. The images or other third party material in this article are included in the article's Creative Commons license, unless indicated otherwise in a credit line to the material. If material is not included in the article's Creative Commons license and your intended use is not permitted by statutory regulation or exceeds the permitted use, you will need to obtain permission directly from the copyright holder. To view a copy of this license, visit http://creativecommons.org/licenses/by/4.0/.

© The Author(s) 2017